The measurement and interpretation of fractal dimensions of the scalar interface in turbulent flows

R. R. Prasad[a] and K. R. Sreenivasan
Mason Laboratory, Yale University, New Haven, Connecticut 06520

(Received 13 July 1989; accepted 6 December 1989)

One of the recently established results concerns the fractal-like properties of surfaces such as the turbulent/nonturbulent interface. Although several confirmations have been reported in recent literature, enough discussion does not exist on how various flow features as well as measurement techniques affect the fractal dimension obtained; nor, in one place, is there a full discussion of the physical interpretation of such measurements. This paper serves these two purposes by examining in detail the specific case of the interface of scalar-marked regions (scalar interface) in turbulent shear flows. Dimension measurements have been made in two separate scaling regimes, one of which spans roughly between the integral and Kolmogorov scales (the K range), and the other between the Kolmogorov and Batchelor scales (the B range). In the K range, the fractal dimension is 2.36 ± 0.05 to a high degree of reliability. This is also the dimension of the vorticity interface. The dimension in the B range approaches (logarithmically) the value 3 in the limit of infinite Schmidt number, and is 2.7 ± 0.03 when the diffusing scalar in water is sodium fluorescein (Schmidt number of the order 1000). Among the effects considered are those of (a) the flow Reynolds number, (b) developing regions such as the vicinity of a jet nozzle or a wake generator, (c) the free-stream and other noise effects, (d) the validity of the method of intersections usually invoked to relate the dimension of a fractal object to that of its intersections, (e) the effect of intersections by "slabs" of finite thickness and "lines" of finite width, and (f) the computational algorithm used for fractal dimension measurement, etc. The authors' previous arguments concerning the physical meaning of the fractal dimension of surfaces in turbulent flows are recapitulated and amplified. In so doing, turbulent mixing is examined, and by invoking Reynolds and Schmidt number similarities, the fractal dimensions of scalar interfaces are deduced when the Schmidt number is small, unity, and large.

I. INTRODUCTION

The notion that a dynamic interface, which is a conceptual surface that separates domains of zero and nonzero vorticity fluctuations, bounds turbulent free shear flows is quite old.[1] One can also define a variety of other surfaces, such as the scalar interface, which is the surface separating regions marked by a passive scalar from those that are unmarked. Isoconcentration surfaces (in reacting or nonreacting flows), isovelocity surfaces, and isodissipation surfaces are other examples. It is useful to understand their properties because of their close connection to processes such as entrainment and mixing.[2,3] In this paper, we are concerned almost exclusively with scalar interfaces.

It appears to have been originally believed that such interfaces are smooth and contiguous, perhaps occasionally multivalued.[4] This view has been questioned more recently.[5] To illustrate this point and facilitate further discussion, we show in Fig. 1 a thin section of dye-marked regions of a turbulent jet obtained at moderate Reynolds numbers. The image shows a number of interesting features,[6-8] but we concentrate here on the interface. It is obvious from Fig. 1 that the boundary is convoluted on a variety of scales (though, perhaps, not too fragmented[8]) and the original concept is

FIG. 1. Two-dimensional laser induced fluorescence image of an axisymmetric water jet. The region imaged extends from 8 to 24 diameters downstream of the nozzle. The nozzle Reynolds number is 4000. A discussion of relevant experimental techniques is given in Sec. II.

[a] Present address: Physics International Co., 2700 Merced Street, San Leandro, California 94577.

 0899-8213/90/050792-16$02.00

too simple-minded, justified only when some coarse graining or instrument smoothing is performed.

The complexity of such surfaces makes it difficult to describe them by means of classical geometry. Mandelbrot[9] (see, also, his other publications cited in Ref. 9) has developed the necessary framework for describing the geometry of such complex shapes; he also recognized that the self-similarity expected to hold in turbulence (according to the conventional wisdom succinctly described by Richardson's rhyme[10]) could permit the use of fractal description of such surfaces. There is now ample evidence that such surfaces are indeed fractal-like[11] in nonreacting as well as reacting flows,[12,13] but not enough discussion exists of how various flow features and measurement techniques affect the fractal dimension obtained; nor is there a full discussion of the physical interpretation of such measurements. This paper serves these two purposes by a detailed examination of the specific case of the scalar interface.

We assume that the readers are familiar with the notion of fractal dimension. Otherwise we refer them to Mandelbrot's original work and, in the particular context of turbulent interfaces, to Ref. 12. In any case, measuring a fractal dimension involves, in some form or another, obtaining the slope of a line in a log–log plot, this being one tangible manifestation of statistical scale similarity. Dynamical similarity *à la* Kolmogorov[14] usually applies only to scales in the inertial subrange, which is ill-defined except at large Reynolds numbers. Since resolution requirements have so far restricted dimension measurements to moderate Reynolds numbers with barely discernible inertial range in *frequency* spectra, it is necessary to ask whether fractal dimension measurements are beset with similar difficulties. It turns out, for reasons yet to be fully understood, that geometric scale similarity (in certain cases) extends to a much wider range of scales than does dynamical similarity of the inertial type. We thus speak of a dimension characterizing most (if not all) of the available scaling range.

For scalars with Schmidt number Sc (the ratio of the kinematic viscosity ν of the fluid to the mass diffusivity of the scalar) far greater than unity, as is the case of a dye mixed in water, diffusion effects become important at scales much smaller than the Kolmogorov scale η [$= (\nu^3/\langle\varepsilon\rangle)^{1/4}$, where $\langle\varepsilon\rangle$ is the average rate of the turbulent energy dissipation]. For these smaller scales, the strain field will be effectively infinite in extent, rendering the scale of the strain field irrelevant; in particular, η plays no role except to act as a cutoff scale analogous to the integral length scale L in the dynamical case. The only important parameter is the turbulent strain rate. Here, two scaling ranges are possible.[15,16] One of them occurs between L and η (to be designated henceforth as the K range), and the other between η and the so-called Batchelor scale[15] $\eta_b = \eta\,\mathrm{Sc}^{-1/2}$; this latter scale range, to be designated as the B range, can be expected to possess a different fractal dimension. The two scaling ranges and the associated fractal dimensions will be discussed separately.

After an initial discussion of experimental facilities in Sec. II, and of image acquisition and data preprocessing in Sec. III, we present the principal results for the dimension appropriate to the K range in Sec. IV; in this section we also discuss procedures for fractal dimension measurements. In Sec. V, we dwell on the so-called method of intersections, this being of interest because the scalar interface resides in three-dimensional space in a complex way and the determination of its fractal dimension by box counting in three dimensions is not always practicable. Furthermore, the method of intersections allows us to measure, with available instrumentation, the fractal dimension of the vorticity interface[12,17] and of the scalar interface in the B range.[16] Dimension results in the B range obtained from finely resolved point measurements are given in Sec. VI. In Sec. VII, we summarize the principal results applicable to fully turbulent flows.

In Sec. VIII, we discuss several factors, in addition to those of Sec. IV, that influence dimension measurements. Some questions addressed are the effect of measuring in regions of a flow that are not fully developed (for example, closer to a jet nozzle than a certain downstream distance), or at low Reynolds numbers; the effect of instrumentation noise and other artifacts associated with free-stream conditions; etc. Another aspect explored is the meaning of results obtained with resolution coarser than is demanded by the smallest scale present. This is examined by taking thicker slices of the flow ("slabs") than dictated by the smallest relevant scale, the extreme case being the projection onto a plane of the entire image (as in conventional schlieren and shadowgraph images). This last case is especially relevant for the measurement of fractal dimensions of natural objects such as clouds and mountain ranges—this being of interest in geophysics and earth sciences—because they are invariably obtained in projections and not sections.

The principal results are that the fractal dimension of the scalar interface in the K range is independent of the flow configuration—at least to a very good first approximation—and that, in the B range, it is almost equal to the dimension of the embedding space. An explanation for the universality of this result has been given in Ref. 3, and recapitulated in Sec. IX. The paper concludes (Sec. X) with a discussion and interpretation of results.

II. FLOW FACILITIES AND INSTRUMENTATION

Several flows—turbulent jets, wakes, boundary layers, and both temporal and spatially developing mixing layers—were studied, but a large fraction of the results presented is for jets.

The water jet emerged from a settling chamber into a large tank of still water through a nozzle of circular cross section and diameter 1.2 cm. The nozzle was contoured according to a fifth-order polynomial to have zero slope and curvature at the entrance as well as the exit, and it was established by running separate air experiments that there were no internal separations in the nozzle. The exit speed was about 35 cm/sec, so that the nozzle Reynolds number was about 4000. The jet was made visible by mixing a small amount of a fluorescing dye (sodium fluorescein) in the plenum chamber, and exciting fluorescence by illuminating a thin section of the flow by a sheet of laser illumination. The laser induced fluorescence (LIF) occurs as a result of the emission of photons when an excited ion or molecule decays

back to its ground state. The lifetime of this process is on the order of 10^{-8} sec. The number of photons emitted, or the fluorescence intensity, is proportional to the number of excited molecules or ions, which in turn is proportional to the number of ground state ions or molecules as well as the illuminating light intensity. If the ground state molecules are too many, the fluorescence intensity decays as the light travels through the fluorescing medium. The fluorescence is then saturated; saturation also occurs if the incident light intensity is not high enough. If, however, the dye concentration is small, there is no significant change in the light intensity as it traverses the medium, and the fluorescence intensity is then directly proportional to the concentration of fluorescent dye. (For relevant references, see Ref. 5.) LIF therefore provides a convenient method for mapping quantitatively the concentration field of a scalar. Much care was taken to ensure that the fluorescence was not saturated. For instance, this was checked by doubling the dye concentration and observing that the peak intensity was correspondingly doubled. Saturation could easily be avoided because of the high power density of the Nd:YAG pulsed laser (2×10^{7} J sec^{-1} per pulse) and small dye concentration (of the order of a few parts per million).

A 6.4 mm diam pulsed beam of light emitted from the YAG laser was directed into the tank of water using two specially coated mirrors and shaped into a sheet of average thickness of 250 μm using lenses A–E (see Fig. 2). The lenses A and B configured as a collimator reduced the diameter of the laser beam from the original 6.4 mm to 2.0 mm. The lenses D and E further reduce, in the plane of the paper (orthogonal to the jet axis), the beam to a sheet about 200 μm wide at the focal point. The effective focal length of this combination is large in order to ensure that the width of the light sheet changes only slowly with distance from the lenses. The light sheet thickness, measured using a linear photodiode array, varied from 200 to 300 μm in the 10 cm range of interest near the jet axis. The cylindrical lens C, oriented perpendicular to lenses D and E, expanded the sheet along the jet axis so as to be able to visualize a region approximately 25 cm high. This covered a jet region extending 8–24 diameters downstream of the nozzle. Using an $f/1.8$ Nikon camera lens of 50 mm focal length, LIF images were obtained on a Photometrics charge-coupled-device (CCD) camera (200 series) with a Videk Megaplus II array of 1320 (vertical) $\times$ 1035 (horizontal) pixels. The pixel resolution turns out to be on the order of 150 μm^2. The CCD camera incorporates a 12-bit digitizer. Data storage and further processing were done on a VAX station II/GPX. As explained in Sec. III, corrections were made for the nonuniform light intensity in the sheet.

The laser pulse duration of about 10 nsec was small enough to freeze fluid motion. However, the fastest CCD camera shutter speed was 0.2 sec. Only a single pulse was captured on each digital frame by operating the laser at the repetition frequency of 5 Hz.

Jet sections were also obtained orthogonal to the axis by rotating the orientation of the laser sheet from along the jet axis to a perpendicular direction. This was done by rotating the cylindrical lenses C, D, and E in Fig. 2 by 90°. The jet

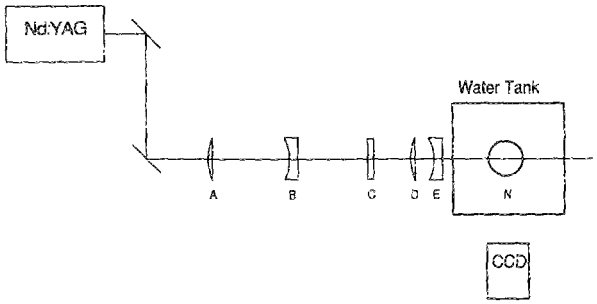

FIG. 2. Schematic diagram showing the apparatus used for imaging water jets. The Nd:YAG laser beam was directed into the water tank using the two mirrors shown. It was shaped into a sheet of about 250 μm thickness using lenses A–E. The lenses are A, spherical, focal length $f = 160$ mm; B, spherical, $f = -50$ mm; C, cylindrical, $f = -6.3$ mm; D, cylindrical, $f = 100$ mm; E, cylindrical, $f = -100$ mm. Also shown in the figure are the nozzle N and the CCD camera.

emerges from the top of the tank and so, to avoid difficulties associated with imaging vertically downwards through the nozzle or upwards through the bottom of the tank, a large mirror was placed at 45° at the bottom of the tank. The camera was then able to image the flow from the side of the tank as before.

The wake was created by rigidly mounting a circular cylinder of aspect ratio 58 and diameter 1 cm, and having the tank of water move past it at a predetermined speed. This method, rather than moving the cylinder in a stationary tank of water, was chosen to avoid possible cylinder vibrations when in motion; it also eliminated the need for elaborate flow management devices upstream of the cylinder. The tank motion was facilitated by mounting it on a hydraulically operated forklift. Typical flow speed was about 15 cm/sec, yielding a wake Reynolds number of about 1500. The fluorescing dye seeped through a thin slot cut along the back stagnation line. In another set of experiments, the cylinder was rotated 180° so that the slot was along the front stagnation line, and the dye wrapped around the cylinder before getting mixed by wake turbulence. Data acquisition was done as for jets. The streamwise extent of the image was between 60 and 75 diameters downstream of the cylinder.

The temporal mixing layer experiments were made by Ramshankar[18] using a 2 m long Thorpe-type[19] apparatus of 15×5 cm cross section. A thin dye layer was established between the two streams. The temporal evolution of the flow resulted in the mixing of the dye, and the interface was studied as a function of time. Essentially the same optical methods were used to map the dye concentration field.

Further measurements were made in a helium jet issuing into ambient air. The LIF technique requires that the jet be seeded with aerosols of a solution of sodium fluorescein in ethyl alcohol. Ethyl alcohol, instead of water, was chosen as the solvent to avoid the aggregation of large sized particles likely to result in water. Aerosols were generated using a six jet TSI atomizer. To limit the effect of particles on the flow, seeding was limited to the absolute minimum consistent with

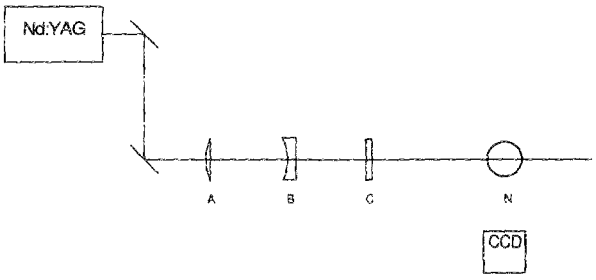

FIG. 3. Schematic diagram showing the apparatus used for imaging helium jets. The laser beam was directed at the jet using the two mirrors as before. It was shaped into a sheet of about 100 μm thickness using lenses A–C. The lenses are A, spherical, $f = 160$ mm; B, cylindrical, $f = -100$ mm; C, cylindrical, $f = -6.3$ mm.

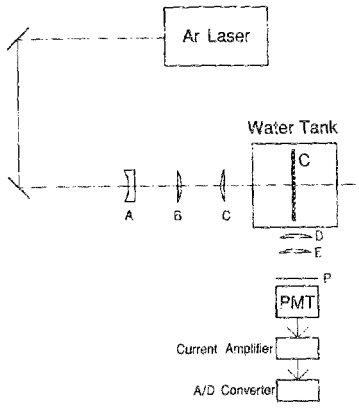

FIG. 4. Schematic of the optical setup used to make point measurements with scale resolution comparable to the Batchelor scale. The spatial dimension of the measurement spot is on the order of 4 μm. This is achieved by a combination of lenses and the pinhole in front of the photomultiplier tube. The focal lengths of lenses L_1–L_5 are, respectively, -25 mm, 300 mm, 500 mm, 400 mm, and 1000 mm. Further details are given in the text.

a reasonable signal/noise level. A schematic diagram of the optical arrangement used is given in Fig. 3.

Measurements were also made in heated air jets where heat was the passive scalar. The nozzle diameter was 5 cm. The jet was supplied by compressed air from two large storage tanks pressurized to 8.3×10^5 N/m^2. After passing through the usual settling chamber, screens and a contraction of area ratio 10, the jet emerged into a chamber 2.5 m high, 3.8 m long, and 2.5 m wide. Measurements were made in this undisturbed chamber. A 3 kW heater mounted in a section upstream of the settling chamber could heat the jet to about 60 °C above the ambient; at the measurement station, the temperature rise was about 5 °C. Measurements were made by a 0.6 μm diam Wollaston wire operated "cold" on a constant current (90 μA) anemometer designed and built in-house. The signal from the anemometer was preconditioned using a DANTEC 55D26 signal conditioner and amplifier, and digitized with 12-bit precision on the MASSCOMP 5000 computer at twice the estimated Kolmogorov frequency. The digitized area was transferred to the VAX station for further processing.

The procedure outlined earlier enables us to obtain well-resolved, quantitative maps of the dye concentration as a function of two space coordinates. A study of the time evolution of the concentration field is also of interest. To do so, images must be acquired at rapid rates. However, the relatively large format of the CCD array and the slow digitization rate (2×10^5 pixels/sec) prevent the acquisition of full frames of data at a rate faster than one every 6 sec. We sacrificed resolution by binning four neighboring pixels to form a single pixel and worked with a smaller image of 400×400 pixels. This allowed the acquisition of images at the rate of one every $\frac{4}{3}$ sec.

The spatial resolution is limited by the pixel size as well as the thickness of the sheet of light. In present experiments, the latter (about 250 μm) proved to be the limitation. Light can be focused much better (see the next paragraph), but not in the form of a sheet of any significant size; this therefore rules out obtaining planar images of nontrivial extent if the goal is to resolve the Batchelor scale, which, in present experiments, is about 4–5 μm. (This assumes[20] a Schmidt number of about 1930. Even though some ambiguity does exist about the precise value, it is believed that the quoted value is of the right order of magnitude.) We therefore aimed at resolving the Kolmogorov scale in planar images, and adjusted the flow Reynolds number and nozzle diameter such that the estimated Kolmogorov scale was on the order of 150 μm midway in the imaged region. The spatial resolution could then be taken in all directions to be between one and two Kolmogorov scales, and we hoped to obtain accurately the fractal dimension characteristic of the K range. If we expressly restrict attention to this range, we may ignore all sub-Kolmorogov scales and think of η as the characteristic thickness of the thinnest section needed. As will be shown in Sec. V, finely resolved point measurements can be used for examining scaling properties in the B range. The corresponding experimental setup used for making such measurements is now described.

The optical setup is shown in Fig. 4; also shown is the orientation of the cylinder (C) whose wake is the object of study here. A 5 mm diam light beam from a continuous argon laser (power output about 7 W) is first expanded into a thicker beam of 60 mm diameter by the combination of spherical lenses A and B, and then focused to a spot of 5.5 μm diameter by means of a convex lens C. The optical signal is collected by a photomultiplier tube (PMT). In the optical path upstream of the photomultiplier tube is a combination of lenses D and E that gives an image enlargement by a factor of 2.5. This combination enlarges the 5.5 μm focal spot in the flow to a size of about 13 μm. Ahead of PMT, a 10 μm diam pinhole (P) is located. This effectively reduces the size of the spot imaged onto PMT to 4 μm. This is the spatial resolution of measurement. Concentration fluctuations are detected as fluctuations in fluorescence intensity, the two being in linear proportion. The optical signal from PMT is passed through a

current amplifier before being digitized by the 12-bit A/D converter on the MASSCOMP 5000 computer. The digitizing frequency is set at 320 kHz, which is well below the limiting digitization rate of 1 MHz of the A/D converter. The photomultiplier tube is quoted by the manufacturer as having good frequency response up to 50 MHz. So the temporal response of the instrumentation is believed to be much better than required for present purposes.

III. IMAGE ACQUISITION AND PREPROCESSING OF DATA

A. Considerations for obtaining high-quality images

The remarks below are specific to jets, but apply with equal force to other flows also.

(i) If the jet is run for long periods of time the tank fluid gets contaminated by the dye and develops background fluorescence. To remove this source of "free-stream" noise, image acquisition was begun soon after the jet settled down to its final state. The tank was flushed out after each run, and replenished with clear filtered water. For all data acquisition, the room was darkened to minimize spurious illumination.

(ii) Two particle filters were used in tandem. However, filters do not remove all particles, and the imaging system will detect some scattered light. Since scattering occurs at the wavelength of the incoming laser and the fluorescence radiation is of a longer wavelength, a long-pass optical filter was used to remove most of the scattered radiation. Figure 5 shows a comparison between the unfiltered and filtered spectra, obtained by the use of a Jarrell–Ash monochrometer with 0.1 nm resolution. The sharp peak near 532 nm in Fig. 5(a) corresponds to the scattered laser radiation from particles. The fluorescence itself peaks at a slightly higher wavelength (545 nm), but is essentially broadband. Hence a filter that cuts off light below a wavelength of 540 nm is desirable. A Corin optics long-pass filter with the cutoff at 550 nm was used. The filter removed all but a fraction of the 532 nm radiation. It also removed some fluorescence intensity [Fig. 5(b)], but this caused no problems because the laser intensity was sufficiently high.

(iii) Digital images were captured directly on the CCD camera and not by first acquiring photographs and subsequently digitizing them. This eliminates uncontrollable errors due to nonlinearities in developing photographic film. The dynamic range of photographic film is also limited (roughly 300 gray levels) compared to that of a digitizing camera (almost 4096 levels on the present camera).

(iv) The CCD array itself has a small amount of dark noise, i.e., the charge collected on each pixel without photon impingement. This dark noise was subtracted from the images.

(v) It is also necessary to take into account variations in laser intensity across the sheet due to the laser itself, and the optics through which the beam passes. This was achieved by uniformly dying the fluid in a smaller tank and capturing the fluorescence intensity without the jet running. (To ensure that the optical path was identical in the two cases, this smaller tank was placed in the middle of the big tank used for other experiments, filled with filtered water in the usual way.) This image was subsequently used for normalizing. The corrected pixel intensity was calculated as

$$\text{corrected pixel intensity} = \frac{(\text{CCD intensity for the jet flow—noise})}{(\text{CCD intensity for the uniformly dyed fluid—noise})}. \quad (1)$$

B. Signal/noise levels

Figure 6 shows a jet section along with a trace of the centerline concentration. There is no indication here of high frequency noise; this can be verified by computing the wavenumber spectra of one-dimensional cuts of concentration field, obtained by Fourier transforming signals of the type shown in Fig. 6 and ensemble averaging over many of them

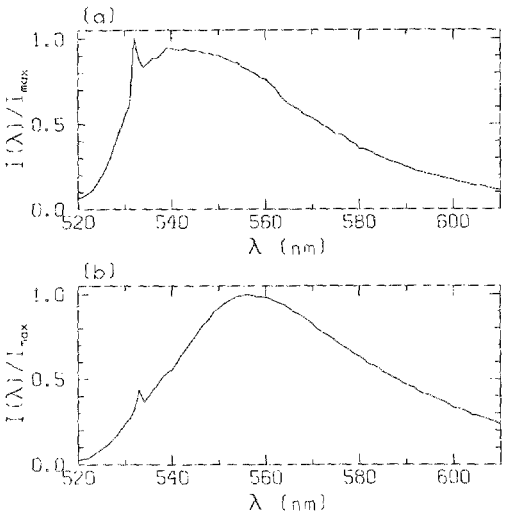

FIG. 5. Comparison of optically (a) unfiltered and (b) filtered fluorescence spectra.

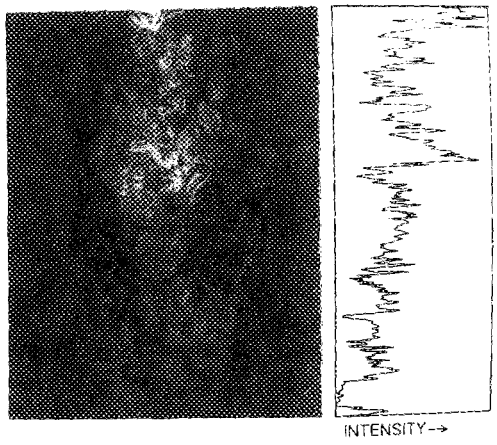

FIG. 6. A two-dimensional LIF image of an axisymmetric jet. On the right is the concentration of the nozzle fluid as a function of the downstream distance x from the nozzle exit. The mean trend in the downstream variation of the concentration is of the type $(x - x_0)^{-1}$, where x_0 is some virtual origin for the self-similar behavior of the jet. The best estimate is $x_0 = -2D$.

(Fig. 7). This was done also for wakes. Figure 8 shows a typical temporal record on the flow axis (see inset), obtained with Batchelor scale resolution, and the corresponding spectral distribution in both K and B regions; the -1 power law, expected from Batchelor's prediction,[15] is highlighted in Fig. 8. All these tests confirm the quality of spatial as well as temporal data. We conclude that there is no significant noise contamination and that elaborate filtering schemes are therefore unnecessary. The main point is that sufficient care must be taken from the very first step of data acquisition.

Several other interesting aspects of power spectra in Figs. 7 and 8 will not be discussed here because they are secondary to our present purpose.

C. Defining the boundary

The definition of the boundary usually entails some edge enhancement techniques. We have investigated standard edge enhancement methods in Ref. 7. One of them, based on the gradient and the Laplacian of the pixel intensity, works well if the intensity change across the edge is sharp (as would be the case if the pixel intensity is zero in some regions and large in others). However, the intensity in turbulent flows does not simply alternate between two fixed values, and even moderate fluctuations within the boundary produce false edges. This problem can be handled in an *ad hoc* manner by using a quantity analogous to the holding time common in turbulence practice,[21] but its arbitrariness cannot always be justified. Another family of techniques involving spatial filtering[22,23] has the problem of smoothing small scale convolutions important to our considerations.

A primary conclusion of Ref. 7 was that, as long as the images were relatively noise-free (as has been demonstrated to be the case here), simple procedures of setting a proper threshold on the pixel intensity is adequate to mark the boundary. The threshold can be set more or less by visual inspection, or can be done by the histogram method of Ref.

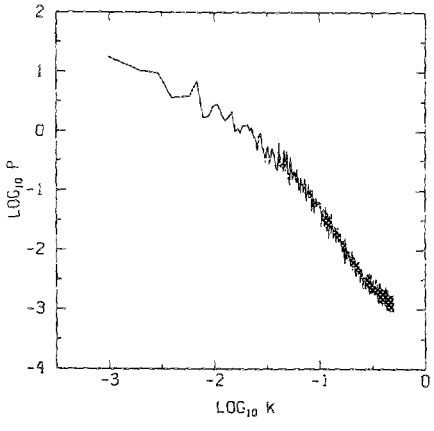

FIG. 7. Wavenumber spectrum of concentration fluctuations in the jet obtained by ensemble averaging 15 realizations, each obtained by Fourier transforming line intersections as in Fig. 6. The smallest wavenumber resolved is comparable to the Kolmogorov scale. The slight upward tendency on the right end is probably caused by the -1 power law inherent to scalar fluctuations (see Fig. 8). The saturation due to the digitizer occurs at much lower levels.

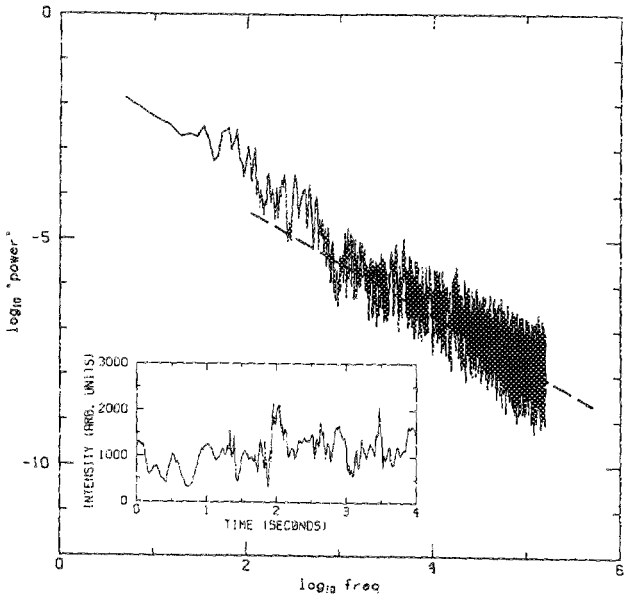

FIG. 8. The frequency spectrum of concentration fluctuations in the wake measured from temporal signals with fine resolution on the wake centerline ($x/D = 75$). The -1 power law characteristic of the B range is marked by a dashed line to the right of the Kolmogorov scale.

7. Under certain conditions, the histogram of intensities over the entire image could be bimodal and the minimum point between the two peaks could serve as a proper threshold. Under certain other conditions, it is better to use the change of slope in a graph of thresholded average intensity (i.e., the average intensity over the entire image calculated using only pixels of intensity above a chosen threshold) against the threshold itself. The conditions under which one or the other of these two schemes works have been described in Ref. 7 and will not be repeated here. For large signal to noise ratios a threshold chosen merely on visual inspection is adequate for most purposes. The computer-drawn boundary of Fig. 1 is shown in Fig. 9; this was obtained by setting the threshold at a brightness level that seemed satisfactory by visual inspection. It is clear that the boundary is quite realistic but, since some minor ambiguities do remain, measurements need to be made for a number of nearby thresholds. We shall presently show these results and mention the effect of using a patently incorrect threshold for interface determination.

IV. DIMENSION RESULTS IN THE K RANGE

A. Algorithms for fractal dimension measurements

One can now apply several techniques to determine the fractal dimension of the boundary so marked. We have used box counting as well as codimension methods. It is worth mentioning that the computer programs for both methods have been checked extensively on several mathematically generated fractal sets of known dimension, and subsequently used by several other investigators elsewhere. The codimension method described in Ref. 12 involves computing the smallest distance from each pixel in the plane to the boundary marked in Fig. 9. The number of pixels $N_c(r)$ within a

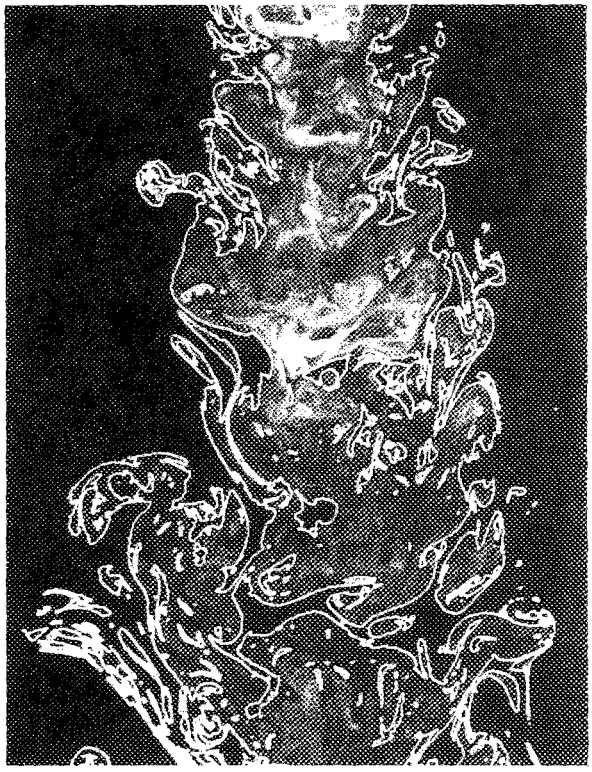

FIG. 9. The two-dimensional jet image of Fig. 1 and the computer generated boundary representing the scalar interface (shown in white).

distance r from the boundary are then counted as a function of r. If the boundary is a fractal, an extensive straight part is expected in log–log plots of $N_c(r)$ vs r. The slope of this straight region is the codimension D_c of the boundary; its fractal dimension is $2 - D_c$. In the box-counting methods, also briefly described in Ref. 12, one covers the whole plane of Fig. 9 with square area elements of varying sizes, and counts the fraction of elements containing the boundary. If the boundary is a fractal, a plot of $\log N(r)$ as a function of the logarithm of the "box" size r should show a straight part, whose negative slope is the fractal dimension.

In the case of a square image of size n^2 pixels, n_b of which are interface pixels, the number of computations required to calculate the dimension in the codimension algorithm is $n^2(n_b + m)$, where m is the number of different values of r's chosen. The first term corresponds to computing the shortest distance from each point to the boundary, and the second to counting the number of pixels within a radius r of the boundary. In box-counting algorithms, however, only $n^2 m$ computations are required. Digital images in most of the present experiments contain about 1.5×10^6 pixels, the interface pixels being typically around 1.5×10^4 and m being typically around 50; the box-counting algorithm is thus far more efficient than the codimension algorithm and is used in almost all measurements described here. The codimension method can be made more efficient by evaluating distances essentially along a vertical or horizontal line (instead of interrogating every pixel in the image). This approximate procedure usually yields acceptable results for objects that are not too highly convoluted. For interfaces in turbulent flows whose geometry is ill-understood, this approximation—even though it appears reasonable *a priori*—cannot always be recommended.

These are not the only methods possible. One can in principle follow the boundary and use dividers of varying segment lengths and obtain the apparent length for various divider lengths. Again slopes in log–log plots yield the fractal dimension. This method is usually difficult for multivalued and fragmented boundaries, but one can use suitable coarse graining at various scales. One such effort[24] has yielded good agreement with present results. If a boundary is evolving dynamically, one can obtain the area swept by the boundary at different closely spaced times, and use the codimension method. We know of no estimates made by this method.

B. Results

Figure 10(a) shows a typical log–log plot of $N(r)$ vs r; we emphasize that the result is typical in that the straight

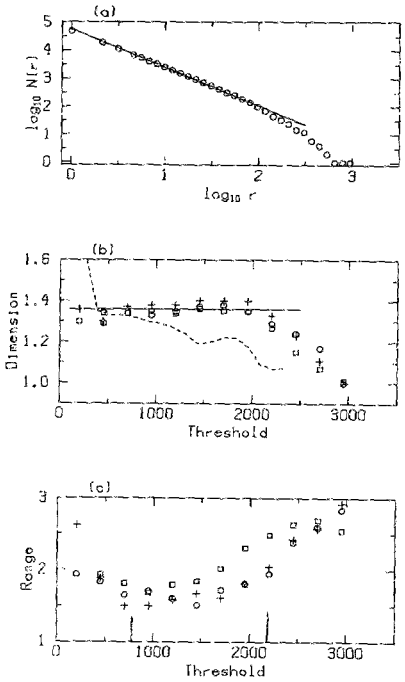

FIG. 10. (a) A typical log–log plot of the number $N(r)$ of square area elements ("boxes") of size r containing the interface versus the box size r. The negative slope of the straight part gives the fractal dimension of the interface section (= 1.36). (b) The fractal dimension plotted as a function of the threshold chosen to determine the interface. The abscissa ranging from 0 to 4096 is the dynamic range of the CCD camera. Also shown in the graph (dashed line) is the variation of the fractal dimension with threshold in digitized photographs, rescaled to match the dynamic range of the CCD camera. Over a large fraction of this range the dimension is essentially independent of the threshold. (c) The scaling range in decades for each threshold. For the Reynolds numbers based on nozzle diameter and velocity in the present set of experiments (about 4000) the typical inner/outer scale ratio is about 200. See the text for remarks on the data within the vertical bars. The different symbols in (b) and (c) correspond to different realizations.

part extending from the smallest scale resolved here to approximately a scale of the order of the nozzle diameter holds provided images are taken carefully as described earlier; sloppier images yield rounded curves and ambiguous results. The slope gives a fractal dimension of 1.36 for the boundary. Figure 10(b) shows the dimension of the boundary as a function of the threshold on the intensity.

It appears from Fig. 10(b) that a wide range of threshold levels exists over which the fractal dimension of the boundary is essentially independent on the threshold. However, Fig. 10(c) shows that the range of scale similarity (that is, the range of scales over which the log–log plot has a straight part) varies with the threshold, and is decidedly smaller for intermediate thresholds. While thresholds near those marking the boundary as in Fig. 9, and those marking regions of intense concentrations, yield log–log plots with unambiguous straight parts, intermediate thresholds (such as close to the average intensity computed over the entire picture) produce log–log plots with reduced scaling, often small enough to be of uncertain value; the range between vertical lines in Fig. 10(c) should therefore be viewed with some caution. On the other hand, in sections perpendicular to the axis, we see no strong variation of the scaling range with the threshold, tempting us to conclude that the behavior seen in Fig. 10(c) is due to inhomogeneities in longitudinal sections. This issue, to which we return briefly in Sec. V B, needs further examination.

Threshold levels correctly marking the scalar interface show log–log regions extending from approximately the large scale L to approximately the Kolmogorov scale η. In general, one can expect on the basis of usual dynamical similarity arguments that only a proper subset of this range, namely, the inertial subrange, exhibits scale similarity. For the present Reynolds numbers, this inertial subrange is small. It is not entirely clear why the geometric scaling is as extensive as observed, but it is this property that enables one to measure the fractal dimension with a high degree of confidence. We shall come back to this issue in Sec. X and take it up in detail elsewhere.

As already remarked, using images obtained on photographic film rather than directly on the digitizer diminishes the threshold range within which the fractal dimension shows reasonable insensitivity. The dashed curve in Fig. 10(b) shows the results of analysis on one of the LIF images acquired through the intermediary of photographic film. (The range was rescaled to match the larger dynamic range of 4096 of the CCD cameras.) Clearly, this procedure introduces undesirable features.

C. Fractal dimension measurements at higher Reynolds numbers

One possible source of concern is that the flow Reynolds number is not high enough. We have obtained LIF images of jets up to Reynolds numbers of about 15 000 and analyzed them in a similar fashion. The scaling in log–log plots was reasonable and slopes were comparable. However, the interpretation of this result is not straightforward because the resolution in these images is poor compared to the Kolmogorov scale, the primary constraint being the thickness of the light sheet. Further discussion is best relegated to Sec. VIII B.

V. THE METHOD OF INTERSECTIONS

A. The additive law

We may now ask how the fractal dimension from planar intersections is related to the fractal dimension D of the surface itself—this being our major interest. The general problem of relating the dimension of a fractal object F to that of its intersections has been discussed in the literature, and some results are available for special cases (see Ref. 25, whose theorems have been generalized in Ref. 26). The equivalent result in the present context, as stated in Ref. 9 (p. 366), relates to the additive properties of codimensions of intersections. Specifically, if S_1 and S_2 are two *independent* sets embedded in a space of dimension d, *and* if codimension(S_1) + codimension$(S_2) < d$, the codimension of the intersection of S_1 and S_2 is equal to the sum of the codimensions of S_1 and S_2. If F is embedded in three-dimensional space and intersected by a plane, the above statement implies that the dimension of the intersected set is one less than that of F.

By making measurements of the fractal dimension in two- and three-dimensional images, we have empirically shown elsewhere[8] that the additive law works well for interfaces in turbulent flows. However, a more convenient way[12,27] of measuring the fractal dimension of such surfaces is to measure the dimension D_s of its two-dimensional section by a thin plane, and use the additive law: The fractal dimension of the surface is simply $D_s + 1$. For this to be correct, the interface must be such that its intersections in different orientations must have the same fractal dimensions.[25,26]

The results so far have shown that the fractal dimension of the boundary in longitudinal (that is, streamwise) sections of turbulent jets is 1.36. Figure 11 shows several orthogonal sections of the jet. The log–log plot analogous to Fig. 10(a) is shown in Fig. 12 for one of the orthogonal sections at an x/D of 21. The slope is essentially the same as that in Fig. 10(a). The scaling range is also as extensive and, as before, the result is sensibly independent of the threshold.

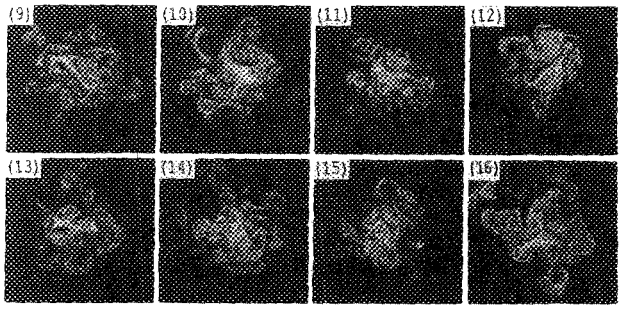

FIG. 11. Eight LIF visualizations orthogonal to the jet axis, from a sequence of 16, obtained 4.6 diameters downstream of the jet axis. The time difference between images is 4/5 sec.

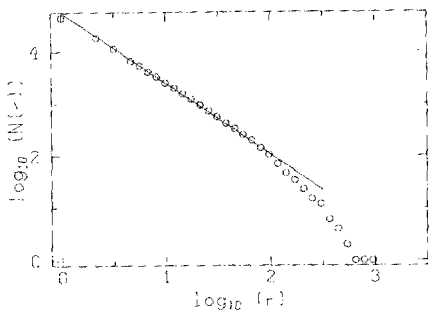

FIG. 12. The log–log plot of the number of boxes $N(r)$ containing the boundary in an orthogonal section ($x/D = 21$) versus the size r of the box. As before, the slope of the straight region in the plot gives the fractal dimension of the boundary. The value of the dimension is the same as that calculated from longitudinal sections.

Figures 13(a) and 13(b) are two independent longitudinal jet sections obtained one and two diameters off axis. The fractal dimension of the boundary in these images is also about 1.36 [Fig. 14(a)], and is independent of the threshold [Fig. 14(b)] in a certain range. It thus appears that the method of intersections should hold, implying that the dimension of the scalar interface in the K range is about 2.36. (The error bars on this number are discussed in Sec. VII.)

It may be useful to remark briefly on why the fractal dimension is independent of the orientation of the intersection plane. This can be expected intuitively to be so for fractally isotropic objects, but flows considered here have a preferential direction. However, strong anisotropic properties of the interface will be confined essentially to the largest scales in the flow—these being on the order of the flow width and larger—and the smaller scales for which fractal-like behavior has been found are expected to be more or less isotropic. One effect of anisotropy appears through unequal ranges of scale similarity in two orthogonal planes, but not on the fractal dimension itself.

B. Line intersections

The principle of additive codimensions also implies that the dimension of line intersections is two less than that of the surface. By using box-counting methods as before, one can compute the fractal dimension of the set of discrete points corresponding to a line intersection of the interface. Figures 15(a) and 15(b) show typical log–log plots for axial and perpendicular sections; Figs. 15(c) and 15(d) show that the dimension does not vary with respect to the position of the line cuts. Figure 15(e) shows that the results are essentially insensitive to the orientation of the line cut. Typical scaling ranges are shown in Fig. 15(f). The mean value of D from these considerations is not far from 2.36 (by making use of the additive principle).

It must be stressed that one-dimensional intersections suffer from lack of sufficient data for obtaining stable statis-

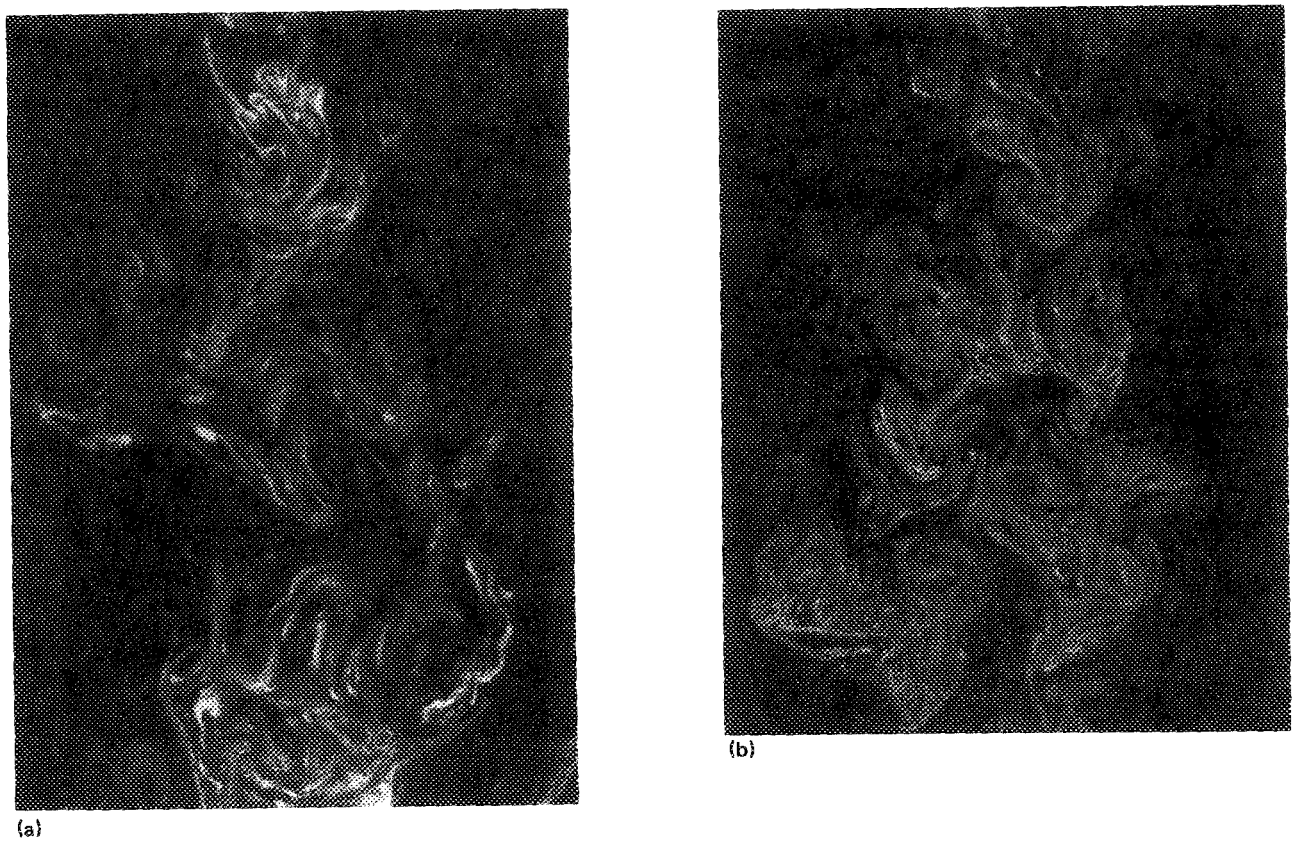

FIG. 13. Two-dimensional laser induced fluorescence visualization along a plane (a) one diameter off axis and (b) two diameters off axis.

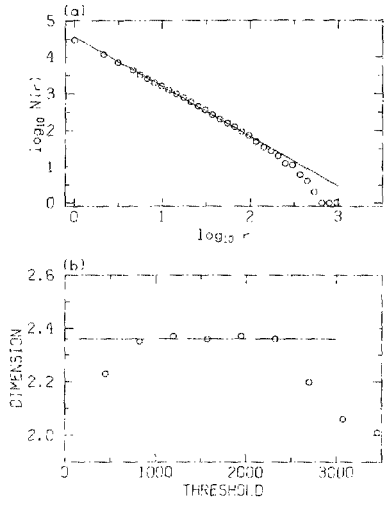

FIG. 14. (a) The log–log plot showing the fractal dimension results for the off-axis sections. (b) The effect of varying the threshold on the fractal dimension estimated from the slope of the log-log plots.

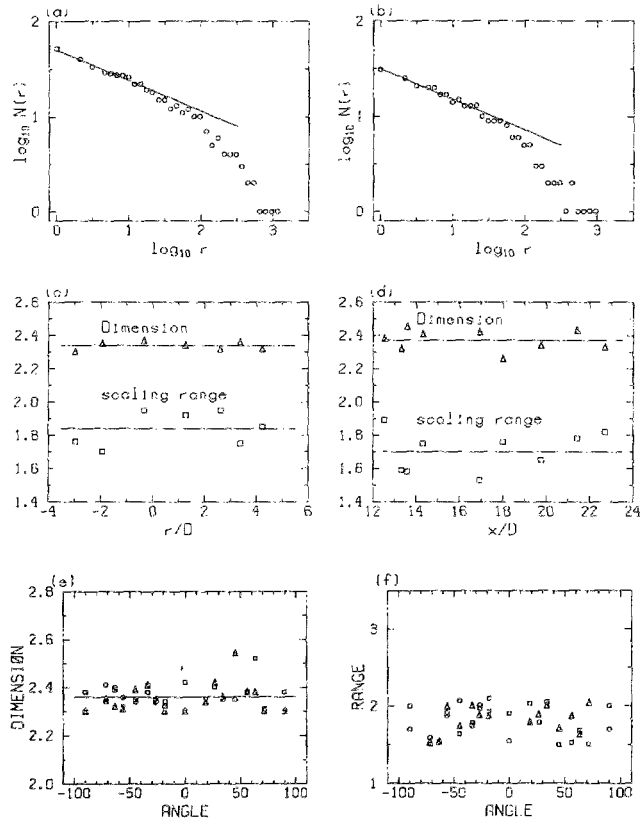

FIG. 15. Typical results from one-dimensional cuts: (a) vertical (that is, axial) and (b) horizontal (that is, perpendicular to the jet axis); (c) and (d) indicate typical variability of the inferred dimension D and the scaling range (in decades) in figures such as (a) and (b) as a function of the position of the one-dimensional cut. The vertical cuts in (c) range from three diameters to the left of the jet axis to five diameters to the right. The horizontal cuts in (d) vary from 12 to 23 diameters downstream of the nozzle; (e) shows typical results from one-dimensional cuts passing through a fixed point as a function of the orientation of the intersecting line. Different symbols correspond to cuts passing through different points in the jet; (f) shows the observed scaling range of cases shown in (e).

tics, this being evident from the scatter in log–log plots as well as from occasional instances where larger box sizes seem to contain a smaller number of points. For very small records it is easy to construct examples where this latter effect is genuine, but it could also arise spuriously depending on the particular way in which the end of data records has to be treated. We have, in most instances, ignored an end piece of the data record if it is not long enough to house an entire box of a given size.

It is difficult to obtain much more data in a single line cut. Sections perpendicular to the flow axis are naturally limited by the flow width, and cannot yield longer records. Data extents of more than a few tens of integral scales in the streamwise direction introduce strong inhomogeneities whose effects remain unknown at present. Long *temporal* records can be obtained with ease, and interpreted as spatial cuts by invoking Taylor's hypothesis (according to which turbulence patterns convect without distortion). This procedure stabilizes statistics, but it also introduces uncertainties[28] whose meaning is unclear. This issue was examined in Ref. 12 where it was concluded that single-point time records lose their fractal-like properties when viewed on very long time scales. It was also concluded that short-time records show fractal-like behavior. The recommended procedure for computing the fractal dimension from one-dimensional temporal records is thus to consider many relatively short segments of data and ensemble average the slopes. One-dimensional data also have the property that a threshold at levels comparable to the mean concentration produce log–log plots with ambiguous or no straight parts. (The situation is worse than that for two-dimensional images discussed in Sec. IV B.) Thus, while one-dimensional data play a supportive role to two-dimensional measurements, care must be exercised in interpreting them in isolation.

The ratio of a typical fluctuation velocity to convection velocity in jets is about two orders of magnitude larger than that for far wakes. Thus Taylor's hypothesis might *a priori* be expected to work better in wakes than in jets; our experience is consistent with this expectation but a thorough study remains to be made. But the observation that Taylor's hypothesis preserves geometric scaling on short time scales is both interesting and useful. In particular, it has been shown[27] that the dimension D is the same for temperature interfaces and dye interfaces (as long as one is restricted to the K range) even though heat diffuses about three orders of magnitude faster in air than does dye in water. We conclude that D is independent of the scalar diffusivity. Furthermore, one-dimensional techniques have enabled us[12,17] to infer that the dimension of the vorticity interface is the same as that of the scalar interface in the K range.

VI. THE SCALING IN THE B RANGE

The fact that Taylor's hypothesis is useful for dimension measurements, albeit with the qualifications mentioned, allows us to obtain from finely resolved point measurements the dimension characteristic of the B range. The experimen-

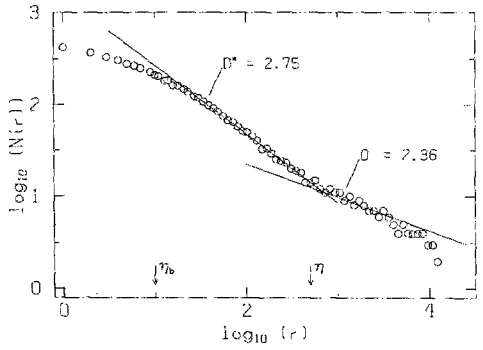

FIG. 16. A typical log–log plot of the number $N(r)$ of line elements ("boxes") of size r containing the interface versus the box size r. The flow is the cylinder wake. The negative slopes of the straight parts give, in the respective scaling regimes, the fractal dimensions of one-dimensional intersections of the boundary. The dimension, corresponding to the slope of the line drawn, in the B range, is about 2.75. That in the K range is about 2.36.

TABLE I. Summary of fractal dimension measurements in classical turbulent flows.

Flow	The K range			The B range[a]
	Method of measurement			
	1-D cuts[b]	2-D images	3-D images	
Round jet	2.36	2.36	2.36	2.7 (Sc = 1930)[c]
Plane wake	2.40	2.36	2.36	2.7 (Sc = 1930)
Plane mixing layer	2.39	2.34	...	...
Boundary layer	2.40	2.38	...	...

[a] All measurements are from one-dimensional cuts, with Taylor's hypothesis.

[b] These measurements for jets and wakes were made both with and without Taylor's hypothesis. Note that one-dimensional measurements often yield slightly higher values for the fractal dimension, but the statistical error bars, deduced from many measurements, are 2.36 ± 0.05. The slight difference from one flow to another may or may not be significant; the present thinking is that they are not.

[c] According to Ref. 20.

tal details for making such measurements were described in Sec. II. Figure 16 shows the usual plot of the logarithm of the number of "boxes" containing the intersection points from one-dimensional cuts through the interface as a function of the box size; the data are from a wake experiment. There are two distinct power law regimes here, one in each of the two ranges. As expected from earlier measurements of Sec. IV, the slope in the latter region is around -0.36, giving the expected value of 2.36 for the fractal dimension in that scale range. (The relatively large scatter is due to the limited duration of the signal, which did not contain too many intersections comparable to bigger boxes.) The B region has a slope of about -0.75, giving the fractal dimension of 2.75. The average slope from several realizations, including from jets, is 2.7 ± 0.03. In Sec. IX we argue that the dimension in the B range is expected to be 3 in the limit of infinite Schmidt number, and that the observed deviation from 3 is a finite Schmidt number effect.

VII. RESULTS FOR OTHER FLOWS AND SUMMARY

Similar experiments in various other flows have been made and fractal dimensions computed as before.[12,18,27] The principal results are summarized in Table I. We should emphasize that, within the uncertainty of measurement, we cannot attach much significance to differences in values estimated from one- and two-dimensional sections, or to variations from one flow to another. It then follows, to a good first approximation, that the fractal dimension of scalar interfaces in the K range is 2.36 ± 0.05 for all fully turbulent flows. Further, this value is the same as the dimension of the vorticity interface. This general result demands an interpretation based on broad considerations. A similar interpretation is necessary for the results in the B range. Before attempting this in Sec. IX, we briefly examine several additional factors influencing fractal dimension measurements.

VIII. ADDITIONAL FEATURES INFLUENCING DIMENSION MEASUREMENTS

A. Fractal dimensions in developing regions and at low Reynolds numbers

Figure 17 shows an axial section of a water jet at a Reynolds number of about 2000. The laminar part of the jet close

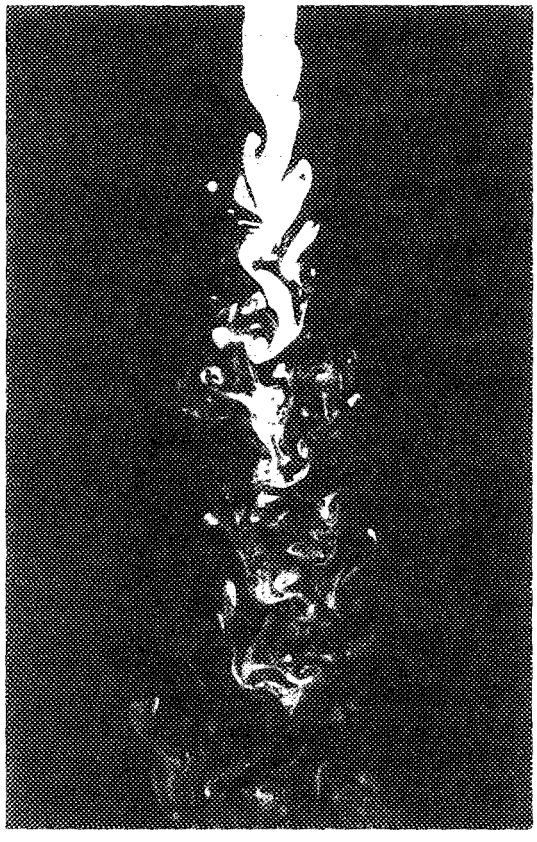

FIG. 17. A typical longitudinal section of the jet at a lower Reynolds number of about 2000 explicitly showing the developing region.

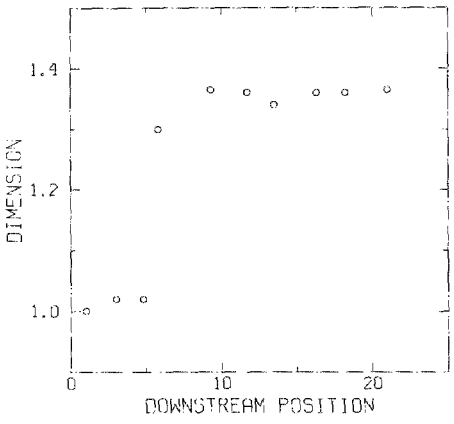

FIG. 18. Measured fractal dimension as a function of the downstream distance normalized by the nozzle diameter.

to the nozzle is clearly visible. At such low Reynolds numbers, the jet is circular in cross-sectional shape as it emerges from the nozzle, and the common sense expectation is that its dimension will be 1. Far enough downstream, however, the jet becomes turbulent and, as we have shown, the cross section there attains a fractal dimension of about 1.36. It is of interest to ascertain the variation of the dimension with axial distance. Typical experimental results are shown in Fig. 18. Low Reynolds number wake data, not shown here, display similar variation along the streamwise direction. This sudden jump in the dimension should, however, be

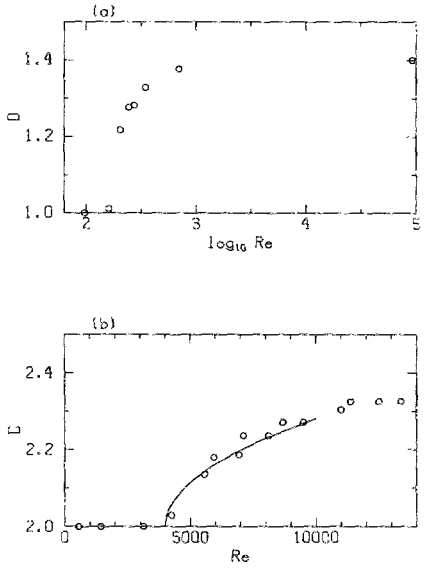

FIG. 19. The variation of the dimension as a function of Reynolds number. (a) Two-dimensional wake, measured by a fixed probe located in the near field. (b) Countercurrent mixing layer, measured from two-dimensional sections (from Ref. 18). The initial rise of the fractal dimension in (b) is closely approximated by a half-power law.

interpreted in a qualitative sense. The reason is that in that transitional regime, the flow at any given distance from the nozzle changes its characteristics from laminar to turbulent in an apparently random way from one realization to another.

Conversely, at a fixed distance from the wake generator, the variation of the fractal dimension as a function of Reynolds number follows the pattern shown in Fig. 19(a). Similar results[18] for the countercurrent mixing layer are given in Fig. 19(b).

An important characteristic of these variations is the abruptness with which the dimension rises. Figure 19(b) shows that the variation is initially, according to a half-power law, reminiscent of typical critical phenomena.

B. Fractal dimensions from thicker sections

As previously remarked, the fractal dimension of scalar interfaces is related to those of sections only when the latter are appropriately thin. From a practical point of view, it is important to establish the effect of taking thicker sections or "slabs" because one often does not have the required instrumentation to obtain thin enough sections—as in the case of the high Reynolds number experiments mentioned in Sec. IV C. An extreme case is one in which no sections are possible and only projections can be obtained. Atmospheric clouds are one good example.

A typical thin section possesses an irregularly shaped boundary with internal holes; the boundary may also be fragmented. The internal foldings and holes get smoothed out in slabs; in the limit of a projection image, we have an object whose interior is perhaps completely filled. The external boundary, however, remains as sharp as that in an intersection—equivalent to viewing the horizon, say, of mountain ranges: One may think of a projection image as being made up of a large number of overlapping thin sections. However, as far as we are aware, no useful mathematical results on this aspect exist; nor, from conversations with many people, do they appear easy to obtain. We therefore present without much comment experimental results on the dimension of the boundary in thick slabs of scalar-marked regions in round jets and plane wakes. A slab of desired thickness is obtained by intersecting the flow by a laser sheet of that thickness. The boundary in each case is marked and its fractal dimension determined; similar analysis is also performed on the projection image. The Reynolds numbers are moderate and comparable in jets and wakes.

A typical visualization of the jet with a 5 mm (20η) thick laser sheet is shown in Fig. 20; also shown is the computer-generated boundary (marked in white) of scalar-marked regions. Similar slabs of different thicknesses were obtained. A projection image was obtained (Fig. 21) by illuminating the flow with two xenon flash lamps (10^{-6} sec/pulse duration) mounted perpendicular to the optic axis of the CCD camera. In all these images, the dimension of the boundary was determined by box counting. Regardless of slab thickness, moderate scaling was observed (over 1.5 to 2 decades) in the usual log–log plots. The dimension results summarized in Fig. 22 show that the fractal dimension decreases as a Gaussian from the "thin sheet" value and

FIG. 20. Visualization of the jet using a 5 mm (20η) thick laser sheet. Also shown is the computer-generated interface, marked in white.

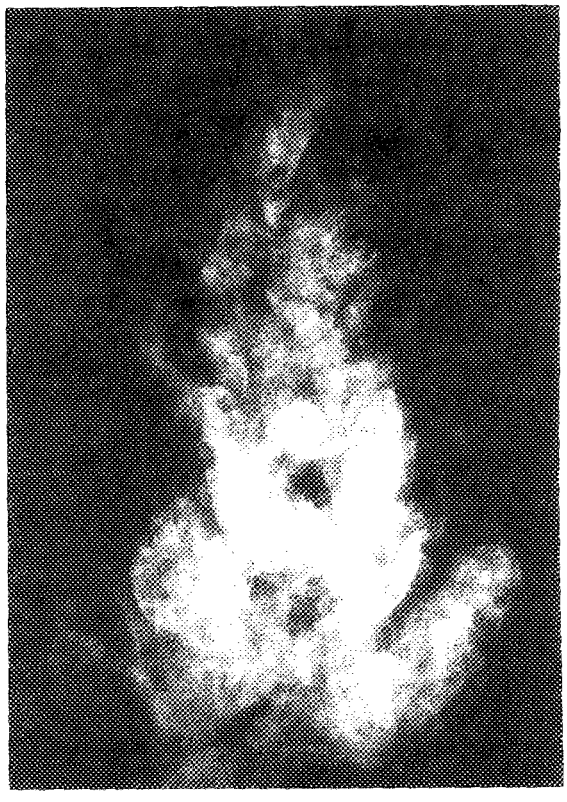

FIG. 21. Projection image of the axisymmetric jet. The jet was visualized using two flash lamps perpendicular to the CCD camera optic axis.

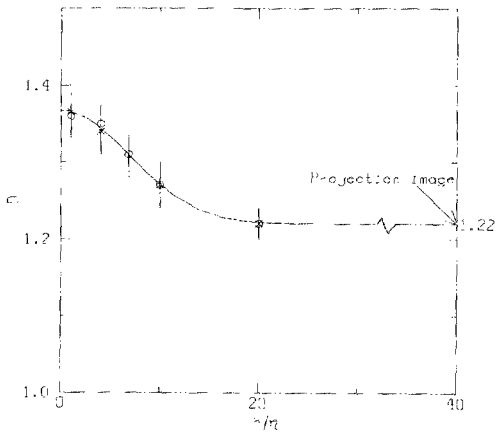

FIG. 22. Fractal dimension D of the scalar interface versus the "slab" thickness h (normalized by η). The circles and crosses represent measured data from jets and wakes, respectively, and the continuous curve is a least squares fit Gaussian (see the text).

asymptotes to that of the projection image. The least squares fit to the Gaussian through the data is

$$D = D_0 + a \exp(-h^2/2\sigma^2), \tag{2}$$

where D_0 is 1.22, a is 0.147, h is the thickness of the slab nondimensionalized by the Kolmogorov thickness, and $\sigma = 6.82$.

To see if this behavior is common, two other flows were studied: the cylinder wake and a buoyant round jet of helium.[29] The wake data shown in Fig. 22 corroborate the same behavior. Although helium jets were not studied extensively, the results were consistent with Fig. 22.

Normalization by the Kolmogorov scale may not produce a universal curve valid for all flows, and the reason it seems to hold for flows studied here may well be that their Reynolds numbers are comparable. While more detailed investigations are needed, it is clear that the dimension obtained with a relatively thick slab will be smaller than the true value, and that the asymptotic value for the projection images is about 1.22 independent of the flow Reynolds number (as long as it sufficiently high).

These observations help us explain the fact that log–log plots at higher Reynolds experiments yielded dimension estimates marginally lower than 2.36, although quantitative assessment would be difficult because of possible nonuniqueness of Fig. 22. They also explain our measurements on cumulus clouds. Photographs of cumulus clouds were taken from the ground with the camera optic axis perpendicular to the ground; appropriate filters were used to eliminate background radiation. The boundary of cumulus clouds, determined by the threshold method, had a fractal dimension of 1.23 ± 0.03, coinciding with that measured for projection images in laboratory flows. We thus infer that the dimension of the boundary of clouds in intersection, if one knew how to obtain it, would be about 1.36. This number is close to the value obtained for clouds by entirely different methods.[30] We infer, at least for cumulus clouds of the size of a few

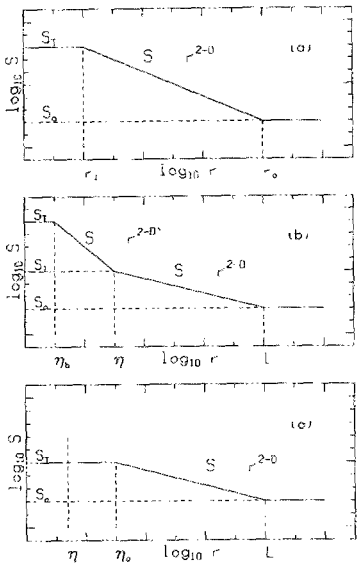

FIG. 23. Schematic variation of the surface area for a fractal-like surface as a function of the resolution. (a) Unity Schmidt number; (b) $Sc \gg 1$; (c) $Sc \ll 1$.

kilometers,[31] that the fractal dimension of the surface is 2.36 ± 0.05. This result is consistent with the laboratory data for fully turbulent flows, again suggesting that a broad principle must be at work. We shall now turn to its discussion.

IX. PHYSICAL INTERPRETATION OF THE INTERFACE DIMENSION

A. The inner and outer cutoffs and the meaning of the fractal dimension

For fractals, the surface area S increases with the resolution of measurement r according to the relation[8]

$$S \sim r^{2-D}. \tag{3}$$

For a "true" fractal, the area is therefore undefined. In all practical circumstances, the scale range over which (3) holds is bounded by cutoffs on both ends [Fig. 23(a)]. In Sec. I, we designated such surfaces as fractal-like. We have already shown that the outer cutoff for surfaces in turbulent flows is expected to be comparable to the integral scale L of turbulence, while the inner cutoff occurs at the smallest relevant scale. For vorticity interfaces, the relevant inner scale is η. The same holds for scalar interfaces when the Schmidt number is unity; we shall consider the nonunity Schmidt number effects shortly. The existence of a finite inner cutoff means that, as the surface area gets measured by covering it with increasingly finer area elements, a point is reached at which convolutions of even finer scales no longer exist, so that, thereafter, the area does not increase with increasing fineness of resolution; instead, it will saturate (abruptly in an ideal situation) at the maximum value corresponding essentially to the inner cutoff. The area S_T of a fractal surface with finite inner cutoff is thus given (to within a constant) by the knowledge of the fractal dimension, and the inner cutoff η which theoretically truncates the power-law behavior. Thus

$$S_T = S_0(\eta/L)^{2-D}, \tag{4}$$

where S_0 is some normalizing area. If the area levels off at L and beyond, S_0 becomes the surface area measured with the resolution equal to L; then $S_0 = L^2$.

We have already remarked that for scalars with Schmidt number greater than unity the relevant inner cutoff occurs at the Batchelor scale η_b. We have also discussed that there are two scaling regimes in this case. Equation (4) therefore needs to be modified. The relation between the apparent area and the resolution of measurement for such surfaces is shown in Fig. 23(b). If S_0 is the area measured with resolution L, S_1 the area measured with resolution η, and S_T is the "true" area measured with resolution η_b, we can write

$$\begin{aligned} S_1 &= S_0(\eta/L)^{2-D}, \\ S_T &= S_1(\eta_b/\eta)^{2-D^*} = S_0(\eta/L)^{2-D}(\eta_b/\eta)^{2-D^*}, \end{aligned} \tag{5}$$

where the fractal dimension characteristic of the B range is D^*. For Schmidt numbers less than unity, the inner cutoff occurs at the so-called Corrsin scale[32] $\eta_c = Sc^{-3/4}\eta$, which is larger than η, and the only relevant exponent is D [see Fig. 23(c)]. The true area in this case is given by

$$S_T = S_0(\eta_c/L)^{2-D}. \tag{6}$$

It is in this sense that the fractal dimension finds a useful role.

B. Mixing of passive scalars: The case of unity Schmidt number

It was shown in Ref. 3 that the characteristic concentration gradient across interfaces is of the order C'/η. Here, C' is a concentration difference characteristic of large scales, such as the root-mean-square value. From these considerations, an expression for the flux of momentum across the interface can be written as

$$\nu S_T(C'/\eta). \tag{7}$$

Defining the characteristic Reynolds number $\mathrm{Re} = U_c L/\nu$ (U_c being the characteristic velocity), we may note that $\eta/L \sim \mathrm{Re}^{-3/4}$, and use Eq. (4) for the interface area S_T to write (after a little algebra) that the

$$\text{flux} = L^2 C' U_c \, \mathrm{Re}^{3(D-7/3)/4}. \tag{8}$$

Note that L, C', and U_c are all independent of Reynolds number.

Now, it is well known that all fluxes (mass, momentum, energy) must be independent of Reynolds number in fully turbulent flows—the so-called Reynolds number similarity. (This is simply a statement of the observed fact that growth rates of turbulent flows of a given configuration are independent of fluid viscosity.) From Eq. (8), Reynolds number similarity requires that

$$D = \tfrac{7}{3}, \tag{9}$$

in rough agreement with measurements (Table I). The same argument carries over to the vorticity interface, yielding the identical result.

We have assumed above that it is appropriate to use a common characteristic concentration gradient everywhere along the interface. This is not strictly true, at least because the interface thickness varies from place to place because of

the spatial intermittency of the dissipation rate ε (which thus produces a fluctuating strain rate). Furthermore, it is implied that the globally averaged dissipation rate is the same as that averaged in the neighborhood of the interface alone. These two issues were addressed in Ref. 3—and, in full detail, in Ref. 33—by resorting to a multifractal representation of the energy dissipation field. The primary result is that Eq. (9) will be modified in the following form:

$$D = \tfrac{7}{3} + 2(3 - D_{1/3})/3. \tag{10}$$

Here, $D_{1/3}$ is the so-called generalized dimension of order $\frac{1}{3}$. In general, q-order "generalized dimensions" D_q are defined as[34]

$$\sum E_r \sim r^{(q-1)D_q}, \tag{11}$$

where E_r is the integral of the dissipation contained in a box of size r, and the summation on the left-hand side of Eq. (11) is carried over all nonempty boxes of sizes r. Elsewhere,[35,36] we have measured the generalized dimensions for the energy dissipation, and in particular shown that $D_{1/3}$ is about 0.96; D is therefore about 2.36, in excellent agreement with experiments.

C. The case of nonunity Schmidt number

If the Schmidt number is small, diffusion effects become important at scalar scales greater than the Kolmogorov scale, and the arguments put forward above do not change except that Eq. (6) must be used instead of Eq. (4) for the surface area. For large Schmidt numbers, the appropriate relation is given by Eq. (5). The flux of a species is then given by

$$\text{flux} = L^2(U_c \cdot \Delta C)\mathrm{Re}^{3(D-7/3)/4}\,\mathrm{Sc}^{\gamma}, \tag{12}$$

where $\gamma = 0.5$ $(D^* - 3)$, for $\mathrm{Sc} > 1$, and $3(D - 7/3)/4$, when $\mathrm{Sc} < 1$. Since the fluxes are expected also to be independent of Sc in fully turbulent flows, Eq. (12) implies that $D^* = 3$ when $\mathrm{Sc} > 1$. This means that interface convolutions on scales between η_b and η are essentially space-filling. No new result is obtained for $\mathrm{Sc} < 1$.

The infinite Schmidt number result gets modified when Sc remains finite (though large). To quantify the effect, we recapitulate that an essential argument used in Ref. 3 is that the concentration gradient across the interface is of the order of C'/η_b—C' being a large scale feature. It turns out[15] that the time taken by the scalar to diffuse down to the Batchelor scale increases logarithmically with the Schmidt number. There is also a corresponding pileup of fluctuation intensity in the scalar patches as the straining by the velocity field continues unabated. The effective concentration gradient is then given by $C'(\ln\sqrt{\mathrm{Sc}})/\eta_b$, and the expression (7) for the flux gets multiplied by the factor $\ln\sqrt{\mathrm{Sc}}$. It is then easy to show that the Schmidt number similarity requires that

$$D^* = 3 - 2\ln(\ln\sqrt{\mathrm{Sc}})/\ln \mathrm{Sc}. \tag{13}$$

In the limit of infinite Schmidt numbers, (13) reduces to $D^* = 3$. For a Schmidt number of 1930, as is believed to be the case for the fluorescing dye,[20] Eq. (13) yields $D^* = 2.65$, quite close to the measured value of 2.7 (Sec. VI).

We reiterate that the present arguments hold in circumstances where the amount of mixing is determined by the large scale, and the surface adjusts itself accordingly. For large eddies to be the controlling factor at infinitely large Schmidt numbers, it is necessary that the Reynolds number must be correspondingly large, the precise condition being that $(\ln \mathrm{Sc})/\mathrm{Re}^{1/2} \gg 1$. As expected on physical grounds, this condition never lets the characteristic gradient across the interface exceed $\Delta C/\eta_b$, where ΔC is the maximum concentration difference in the flow.

X. DISCUSSION AND CONCLUSIONS

We have experimentally measured one simple geometric feature, namely, the fractal dimension, of scalar interfaces in turbulent flows. We have used various imaging techniques and a good part of the paper is devoted to describing the nature of experimental measurements; the belief is that they contain information useful in several contexts in turbulence. In the process, we have established the validity of the method of intersections (at least from three to two dimensions).

In contrast to the scaling range in frequency spectra, the scaling in box-counting methods extends (in two-dimensional images) over most of the available range; for example, in the K range, it extends almost all the way from the Kolmogorov scale η to the integral scale L. Experiments at very high Reynolds numbers will be required to make more precise statements, but such measurements are still lacking and are unlikely to be made with adequate resolution in the near future. Our own unpublished experiments at higher Reynolds number jets confirm the main result on the dimension, but shed little light on the scaling range as a result of resolution problems. One-dimensional measurements at high Reynolds numbers using Taylor's hypothesis have confirmed the main result, but we must emphasize that they call for cautious interpretation unless backed by two-dimensional measurements. At any range, it is clear that the scaling for the interface is more extensive than the classical inertial subrange in the frequency spectra of the longitudinal velocity spectrum, the latter generally extending from about $20f_\eta$ to almost f_L, where f_η and f_L are the Kolmogorov and integral scale frequencies, respectively. The primary difference in the interface measurements is not at the large scale end but at the small scale end, where it approaches the Kolmogorov scale in the K range. Two possible explanations of what seems to be the merger of the inertial and dissipative ranges are the following.

(a) We have considered only flow extents of linear size of order L, and not many hundreds of L's characteristic of spectral measurements. Thus any nonscaling sample-to-sample fluctuations included in the latter do not influence the scaling in the present method. The source of these fluctuations and their relevance to overall flow dynamics are currently being examined.

(b) The scaling is invariably better in two dimensions than in one, and it is possible that two- and three-dimensional spectra display better scaling than do one-dimensional spectra.

These notions are at present based only on preliminary

work, and much needs to be done before they can be considered established.

In spite of these remarks, we believe that the dimension results presented here are solid. For passive scalars of unit Schmidt number, the interface dimension is 2.36 ± 0.05 independent of flow configuration as long as the flow is fully turbulent. From Refs. 12 and 17, the fractal dimension of the vorticity interface is also 2.36. The fact that the two interfaces have the same dimension is consistent with the notion that the scalar is dynamically passive, and that its geometric features are set by turbulence dynamics. If the Schmidt number is small, the same fractal dimension is believed to hold except that the inner cutoff occurs close to the Corrsin scale η_c instead of close to η. For large Schmidt numbers, the dimension in the K range is 2.36 also, but a different scaling occurs between η and the Batchelor scale η_b and is characterized by its own dimension. The scalar convolutions in this range are essentially space-filling (that is, the dimension is 3), but finite Schmidt number corrections reduce the dimension to about 2.7 even when the Schmidt number is of the order 1000. On the basis of Reynolds number and Schmidt number similarities, these results have been given some phenomenological explanation in terms of turbulent mixing.

This explanation is essentially heuristic, and it is useful to ask if the main dimension results can be deduced from some generic properties of the equations of motion. If the effect of viscosity and diffusivity are benign and appear only through the imposition of cutoffs, these results must be associated with the inviscid and nondiffusive equations rather than the Navier–Stokes equations and the corresponding scalar equations including diffusivity. In spite of important lines of inquiry,[37,38] things remain unclear.

The fractal dimension is a useful entity[2,3] in the context of turbulent mixing and entrainment of the ambient fluid. It gives, however, and incomplete information on the surface. This is illustrated graphically in Fig. 11, which shows several images in a temporal sequence taken perpendicular to the jet axis. The variety of shapes seems endless, and yet all of them have practically the same dimension. A more detailed description of the interface is *via* multifractals,[34,39–41] briefly introduced through the q-order moments in Sec. IX. Such measurements on the interface are possible in principle because the information is already contained in the images acquired here but, as shown by a preliminary effort,[18] several practical difficulties surround their accurate determination.

ACKNOWLEDGMENTS

This work has had much valuable input from many different people, and it impossible to acknowledge them all. We should, however, single out R. Ramshankar and C. Meneveau. We have also benefitted from a discussion with Professor P. E. Dimotakis and P. E. Miller.

Part of the writing was done while KRS held the Guggenheim fellowship and was a visiting professor at Rockefeller University. The financial support from AFOSR enabled us to start the work, and grants from DARPA (URI) and NSF have sustained the effort.

[1] S. Corrsin, NACA Wartime Report W-94, 1943.
[2] F. C. Gouldin, AIAA J. **26**, 1405 (1988).
[3] K. R. Sreenivasan, R. Ramshankar, and C. Meneveau, Proc. R. Soc. London Ser. A **421**, 79 (1989).
[4] O. M. Phillips, J. Fluid Mech. **51**, 97 (1972); S. T. Paizis and W. H. Schwarz, *ibid.* **63**, 315 (1974).
[5] P. E. Dimotakis, R. C. M. Lye, and D. A. Papantoniou, Phys. Fluids **28**, 3185 (1983).
[6] R. R. Prasad, C. Meneveau, and K. R. Sreenivasan, Phys. Rev. Lett. **61**, 74 (1988).
[7] R. R. Prasad and K. R. Sreenivasan, Exp. Fluids **7**, 259 (1989).
[8] R. R. Prasad and K. R. Sreenivasan, to appear in J. Fluid Mech.
[9] B. B. Mandelbrot, *The Fractal Geometry of Nature* (Freeman, San Francisco, 1982).
[10] L. F. Richardson, *Weather Prediction by Numerical Process* (Cambridge U.P., Cambridge, 1922).
[11] By using the term fractal-like, we are explicitly recognizing (following Ref. 12) the finite bounds or cutoffs for the scale-similar behavior characteristic of fractals. More on this will follow in Sec. IX.
[12] K. R. Sreenivasan and C. Meneveau, J. Fluid Mech. **173**, 357 (1986).
[13] D. Liepmann and M. Gharib, Bull. Am. Phys. Soc. **32**, 621 (1987); F. C. Gouldin, S. M. Hilton, and T. Lamb, in *22nd International Symposium on Combustion* (The Combustion Institute, Pittsburgh, 1988), p. 541; M. Murayama and T. Takeno, *ibid.*, p. 551; W. C. Strahle and J. I. Jagoda, *ibid.*, p. 561; P. J. Goix, T. G. Shephard, and M. Trinite, Combust. Sci. Technol. **63**, 275 (1989); T. C. Chen and L. P. Goss, AIAA Paper No. 89-2529, 1989; J. Mantzaras, P. G. Felton, and F. V. Bracco, Combust. Flame **77**, 295 (1989). For dimension estimates from numerical calculations, see, for example, A. J. Chorin, Commun. Math. Phys. **83**, 517 (1982).
[14] A. N. Kolmogorov, C. R. Acad. Sci. URSS **30**, 299 (1941).
[15] G. K. Batchelor, J. Fluid Mech. **5**, 113 (1956).
[16] K. R. Sreenivasan and R. R. Prasad, Physica D **38**, 322 (1989).
[17] M. S. Fan and K. R. Sreenivasan (private communication).
[18] R. Ramshankar, Ph.D. thesis, Yale University, 1988; in *Proceedings of the Conference on Chaos in Fluid Flows, La Jolla*, edited by K. N. Ghia (ASME, New York, 1989), p. 84.
[19] S. A. Thorpe, J. Fluid Mech. **32**, 963 (1968).
[20] B. R. Ware, D. Cyr, S. Gorti, and F. Lanni, in *Measurement of Suspended Particles by Quasi-Elastic Light Scattering*, edited by B. Dahneke (Wiley, New York, 1983), p. 255.
[21] R. A. Antonia, Annu. Rev. Fluid Mech. **13**, 131 (1981).
[22] D. M. Marr and E. Hildreth, Proc. R. Soc. London Ser. B **207**, 187 (1980).
[23] J. Canny, IEEE Trans. **8**, 679 (1986).
[24] R. Everson, L. Sirovich, and K. R. Sreenivasan, to appear in Phys. Lett. A.
[25] J. M. Marstrand, Lond. Math. Soc. **3**, 257 (1954).
[26] P. Mattila, Ann. Acad. Sci. Fenn. Ser. A I Math **1**, 227 (1975).
[27] K. R. Sreenivasan, R. R. Prasad, C. Meneveau, and R. Ramshankar, J. Pure Appl. Geophys. **131**, 297 (1989).
[28] A. S. Monin and A. M. Yaglom, *Statistical Fluid Mechanics*, Vol. 2 (MIT Press, Cambridge, 1971).
[29] K. R. Sreenivasan, S. Raghu, and D. Kyle, Exp. Fluids **7**, 309 (1989).
[30] S. Lovejoy, Science **216**, 185 (1982).
[31] We expect that for clouds which are thousands of kilometers in extent the situation may be quite different, although the original data of Lovejoy do not support such an expectation.
[32] S. Corrsin, Phys. Fluids **7**, 1156 (1964).
[33] C. Meneveau and K. R. Sreenivasan, Phys. Rev. A **41**, 2246 (1990).
[34] H. G. E. Hentschel and I. Proccacia, Physica D **8**, 435 (1983).
[35] C. Meneveau and K. R. Sreenivasan, Nucl. Phys. B (Proc. Suppl.) **2**, 49 (1987).
[36] C. Meneveau and K. R. Sreenivasan, submitted to J. Fluid Mech.
[37] A. J. Chorin, Department of Mathematics, Univ. Berkeley, California, Report PAM-425, 1988.
[38] P. Constantin, in *Proceedings of the Newport Conference on Turbulence*, edited by L. Sirovich and S. Orszag (Springer, New York, 1990).
[39] B. B. Mandelbrot, J. Fluid Mech. **62**, 33 (1974).
[40] U. Frisch and G. Parisi, in *Predictability in Geophysical Fluid Dynamics and Climate Dynamics*, edited by M. Ghil, R. Benzi, and G. Parisi (North-Holland, Amsterdam, 1985), p. 84.
[41] T. C. Halsey, M. H. Jensen, L. P. Kadanoff, I. Proccacia, and B. I. Shraiman, Phys. Rev. A **33**, 1141 (1986).